Aerodynamic Decelerator Systems Technology Conferences
30 Mar - 2 Apr 2015, Daytona Beach, FL
23rd AIAA Aerodynamic Decelerator Systems Technology Conference

10.2514/6.2015-2117

Flight Testing of Autonomous Parafoils Using Upper Surface Bleed Air Spoilers

E. Scheuermann[1], M. Ward[2], M. Cacan[3], M. Costello[4]
Center for Advanced Machine Mobility, Georgia Institute of Technology, Atlanta, Georgia 30332

K. Bergeron[5]
US Army Natick Soldier Research, Development, and Engineering Center, Natick, MA 01760

Upper surface bleed air spoilers are a novel control mechanism for guided airdrop systems. In contrast with conventional trailing edge deflection mechanisms, upper surface bleed air spoilers have been shown to be extremely effective for both lateral (turn rate) and longitudinal (glide slope) control of parafoil aircraft. Bleed air spoilers operate by opening and closing several span-wise slits in the canopy upper surface thus creating a virtual aerodynamic spoiler from the stream of expelled ram air. The work reported here investigates the autonomous landing performance of parafoil aircraft in both computer simulation and flight testing using upper surface bleed air spoilers exclusively for lateral steering control and combined lateral and longitudinal control. Additionally, a novel in-canopy bleed air actuation system has been designed and successfully flight tested on a variety of larger parafoil aircraft ranging in payload weight from 300 lb to nearly 1000 lb. The in-canopy system consists of several small, specifically designed winch actuators mounted inside the parafoil canopy capable of opening one or more upper surface bleed air spoilers completely independent of the system AGU. Details of the in-canopy hardware, unique internal rigging structure, and resulting flight performance using the in-canopy system are also presented with excellent results.

I. Introduction

Autonomously guided airdrop systems have revolutionized the notion of aerial delivery by significantly improving airborne cargo landing accuracy and precision. This improvement comes in large part due to the application of steerable ram-air parafoil canopies and sophisticated guidance, navigation, and control (GN&C) algorithms providing the unique capability of such systems to penetrate atmospheric winds and thus maintain close proximity to the target area throughout descent and landing. However, the act of consistently delivering such cargo with pinpoint accuracy and precision is extremely difficult. Limited sensing capability and available control channels combined with variable atmospheric conditions represent some of the biggest challenges airdrop system designers have faced for decades. Furthermore, a growing need exists for improved airdrop system performance where hyper-accurate landing capability is required to ensure continued mission success. These missions may include urban or rooftop targets, moving vehicles or ships, mountainous terrain, and rapidly changing battlefronts. Accordingly, new autonomous airdrop system methodologies and techniques are needed to meet these demands.

Current autonomous parafoil and payload systems are typically controlled by asymmetric deflection of the canopy left and right trailing edges (left and right brakes) providing an effective means of lateral steering control [1-10]. Other methods for achieving lateral steering control include in-flight rigging angle adjustment [11] and lateral weight shift [12]. Although systems employing these control mechanisms have demonstrated substantial improvement in landing accuracy over similarly sized unguided systems, their limited number of available control

[1] Graduate Research Assistant, Student Member AIAA.
[2] Research Engineer, Member AIAA.
[3] Graduate Research Assistant, Student Member AIAA.
[4] Professor, Guggenheim School of Aerospace Engineering, Woodruff School of Mechanical Engineering, Associate Fellow AIAA.
[5] Senior Research Aerospace Engineer, Senior Member AIAA.

channels makes them highly susceptible to wind gusts and other unknown atmospheric conditions near the target area, often leading to large errors in landing position.

In recent years, several researchers have demonstrated that adding longitudinal control (i.e. glide slope control) to directly alter the parafoil glide ratio in-flight is a very effective means for reducing impact point errors and greatly improving landing accuracy [12-17]. Currently, several mechanisms capable of effective glide slope control have been identified including longitudinal weight shift [12], symmetric brake deflection for airspeed control [13], in-flight adjustment of the canopy incidence angle [14-15], and actuation of upper surface canopy spoilers [16-17]. This last mechanism, shown in Figure 1, is the subject of the current work and consists of several span-wise slits in the upper surface of the parafoil canopy that, when opened, create a virtual spoiler by releasing pressurized air from within the canopy cell. Much like conventional aircraft, opening of these spanwise slits creates a disturbance in the airflow over the parafoil wing resulting in a localized perturbation of the associated aerodynamic forces and moments. Depending on the number and location of each open upper surface spoiler slit relative to the canopy centerline, significant changes in vehicle lateral and longitudinal dynamics have been demonstrated including spiral turns and reductions in system glide ratio by over 70% [17]. Given the relatively small area of the upper canopy surface affected during opening of these spanwise slits, upper surface bleed air spoilers require significantly less actuation force compared with that needed to deform large portions of the canopy trailing edge. As a result, substantial actuator size, weight, and cost savings are possible using bleed air spoilers for control, enabling new and innovative ideas that break the paradigm of payload borne actuation. To date, nearly all autonomously guided parafoil and payload aircraft are designed with control actuators (i.e. winches) mounted on or near the payload and one or more control lines connected to various points on the canopy surface. Although human skydivers and parachutists are physically constrained to use only their arms for control while suspended from the canopy rigging, autonomous systems are in no way restricted to operate under such constraints.

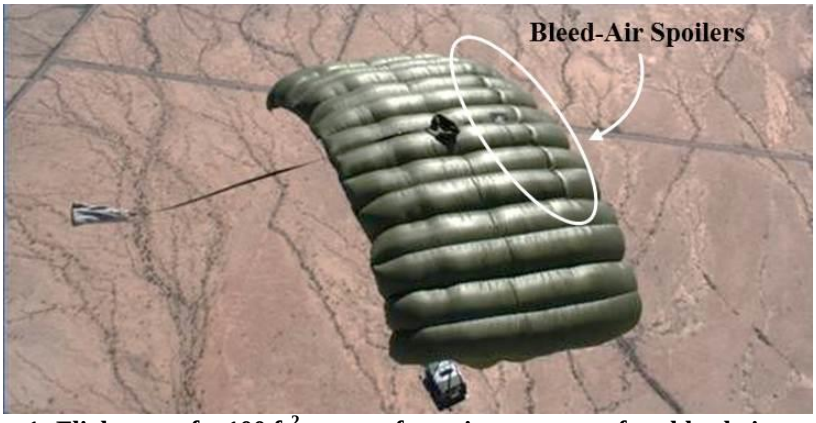

Figure 1: Flight test of a 100 ft^2 canopy featuring upper surface bleed air spoilers.

The research reported here investigates the use of upper surface bleed air spoilers for improved landing accuracy of parafoil and payload aircraft using both lateral steering control and combined lateral and longitudinal steering control techniques. A description of the upper surface canopy spoiler mechanism and combined lateral and longitudinal control logic is presented including autonomous landing accuracy statistics computed from high fidelity computer simulations and experimental flight test results using a small scale parafoil and payload system test vehicle. Additionally, design and development of a novel in-canopy bleed air actuation system is presented including flight test results utilizing the in-canopy hardware on a variety of large parafoil canopies including the MC-4/5.

II. Bleed Air Control

Upper surface bleed air spoilers are defined as a series of spanwise slits introduced across the upper surface of the individual cells in a parafoil wing. Although conventional aircraft spoilers are designed as retractable flaps extending from the upper surface of the wing, bleed air spoilers make use of vented high pressure air from within the canopy itself to create a virtual spoiler from the stream of expelled air. Figure 2 provides a cross-section illustration of the upper surface bleed air control mechanism. Here the upper surface bleed air opening is located at approximately $0.25c$ back from the leading edge where c represents the mean airfoil chord. It should be noted that

moving the bleed air opening closer to the leading edge of the wing does increase the effectiveness of the spoiler. However, additional complications with keeping the cell properly inflated during flight have been documented when the slits are positioned at distances of $0.15c$ or less from the canopy ram air opening [17].

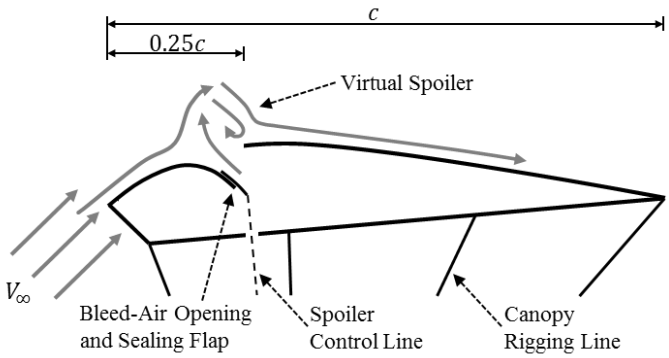

Figure 2: Upper surface bleed air spoiler cross-section view.

Each upper surface bleed air spoiler is actuated by pulling down at the center of the leading edge side of the slit. Additionally, a small piece of fabric or sealing flap is added to the actuated edge of the slit to help prevent air leakage when the spoiler is closed. When not actuated, the spanwise tension and internal pressure from within the canopy cell is sufficient to force the upper surface spoiler closed allowing the airflow over the parafoil wing to reattach and return to its unperturbed state. Asymmetric actuation (opening) of the bleed air spoilers with respect to the canopy centerline creates a moment about the vertical axis of the vehicle enabling lateral-steering control while symmetric spoiler actuation contributes primarily to changes in vehicle glide ratio.

All previous realizations of bleed air control mechanisms include several control lines that run from each bleed air opening down through the lower surface of the parafoil canopy before joining and connecting to one or more winch actuators located on the payload or within the system autonomous guidance unit (AGU). This configuration is shown in Figure 3. In practice, this actuation strategy is similar to that of conventional trailing edge brake deflection and most compatible with existing airdrop hardware where control line attachment points are simply moved from the canopy trailing edge to the upper surface bleed air opening.

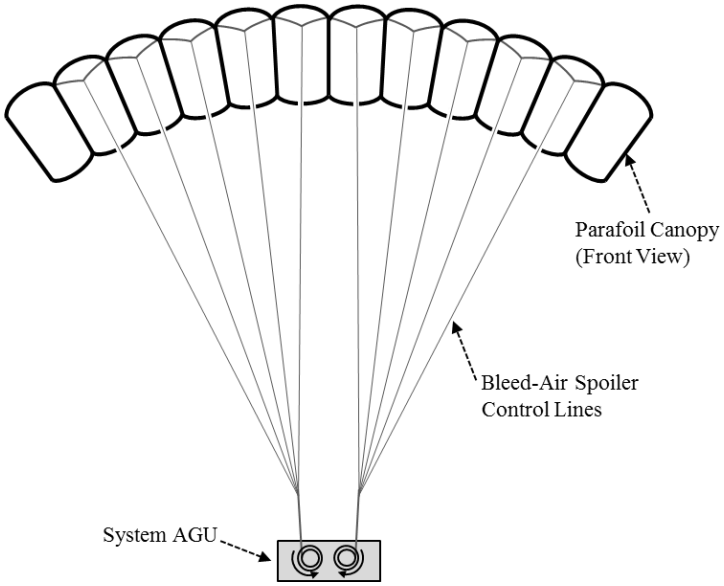

Figure 3: Canopy front view showing bleed air actuation from system AGU.

One of the primary advantages to using upper surface bleed air spoilers for control is the ability to compensate for imperfect approach trajectories via longitudinal control simply by opening or closing the upper surface bleed air vents. However, it must be noted that changes in vehicle turn rate and glide slope are inherently coupled in systems using bleed air control. Asymmetric opening of the upper surface spoilers about the canopy centerline results in not only significant turn rates, but also increases the vehicle descent resulting in a lower glide ratio throughout the turn. As a result, an accurate mapping of the canopy turn rate and glide slope coupling for various amounts of symmetric and asymmetric spoiler openings is needed to accurately command the system to its intended target.

III. Guidance, Navigation, and Control (GN&C) Algorithm

The guidance, navigation, and control (GN&C) algorithm is responsible for path planning, estimating relevant system states and atmospheric conditions, and determining the necessary system inputs to track the desired trajectory. The following sections address each of these tasks individually and describe the logic used during all autonomous flights presented within this paper. Note the basic algorithm presented here shares many of the same features with state-of-the-art autonomously guided systems discussed in literature [1-10]. Where applicable, additional discussion has been included detailing the implementation of lateral and longitudinal control using upper surface bleed air spoilers.

A. Guidance

The guidance algorithm employed here consists of a T-style approach and is divided into 4 separate phases – initialization, loiter, final approach, and terminal guidance. In order to simplify the required calculations, all path planning is performed within the wind fixed or wind relative reference frame (denoted with subscript WF) shown in Figure 4. Derivation of the wind fixed reference frame, originally introduced by Goodrick, Pearson, and Murphy [18] and later by Jann [5], consists of a translation based on the integral of the wind profile and vehicle sink rate followed by a rotation from the inertial frame such that the $\vec{I}_{WF}$ axis points directly downwind. Although wind profile and sink rate may vary with altitude and control inputs, the transformation from the inertial frame to the wind fixed frame can be simplified using filtered estimates of the current wind and treating the parafoil sink rate as constant. Accordingly, Equations 1-3 detail the proposed simplifications and calculations required for transformation from inertial to wind fixed coordinates. Note that (x, y) are the current vehicle coordinates relative to the inertial frame, (x_{WF}, y_{WF}) are the transformed wind fixed coordinates, T_{rem} is an estimate of the time remaining in flight, $(V_{W,x}, V_{W,y})$ are the estimated wind vector components along the north and east directions, and ψ_W is the estimated wind vector direction. Note vertical winds are not considered in the computation of the wind fixed frame.

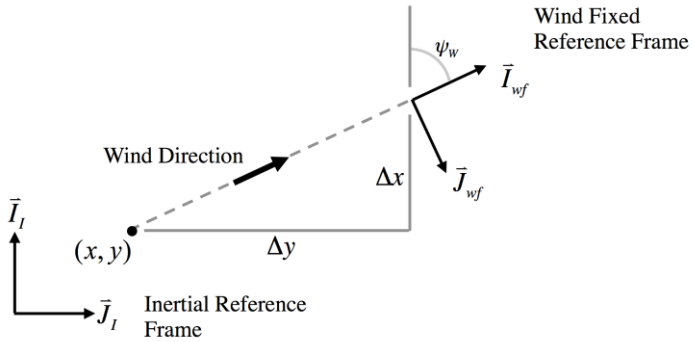

Figure 4: Wind fixed reference frame.

$$T_{rem} = \frac{h}{\dot{z}} \tag{1}$$

$$\begin{Bmatrix} x_{WF} \\ y_{WF} \end{Bmatrix} = \begin{bmatrix} \cos\psi_W & \sin\psi_W \\ -\sin\psi_W & \cos\psi_W \end{bmatrix} \begin{Bmatrix} x + T_{rem}V_{W,x} \\ y + T_{rem}V_{W,y} \end{Bmatrix} \tag{2}$$

$$\psi_W = \tan^{-1}\left(\frac{V_{W,y}}{V_{W,x}}\right) \tag{3}$$

Initialization

The objective of the initialization phase is to estimate wind magnitude, wind direction, and vehicle airspeed in order to properly initialize the navigation filter used throughout the remainder of the flight. During initialization, a constant asymmetric spoiler input is commanded allowing the system to fly at least one complete circle. Typical turn rates commanded during initialization are between 10-15 deg/s. Using the resulting GPS velocity measurements, the task of estimating the horizontal wind components and system airspeed can be cast as a linear regression problem assuming each wind component and the vehicle airspeed are constant throughout the entire open-loop turn. Further detail regarding the solution of the linear regression problem can be found in [19].

Loiter

The loiter (i.e. energy management) phase of the guidance algorithm consists of a series of figure eight turns performed just downwind of the intended target within the wind fixed reference frame. Each end of the figure eight path is comprised of homing targets located at either end of a T-shaped pattern as shown in Figure 5 where the vertical section of the T-shape is collinear with a line drawn directly downwind from the target. Although each homing target is fixed within the wind fixed frame according to the specified geometry of the T-shape, computation of the wind fixed reference frame automatically "tilts" each loiter target into the wind using the current wind estimate. For simplicity, all path planning between loiter targets is performed using Dubins paths [20] consisting of two constant radius turns joined by a single linear segment. Note the final path tangent is always fixed to point directly upwind as indicated in Figure 5. Although each turn during loiter can be made in either direction, the guidance algorithm is configured to select the sequence of initial and final turns resulting in the shortest total distance between homing targets.

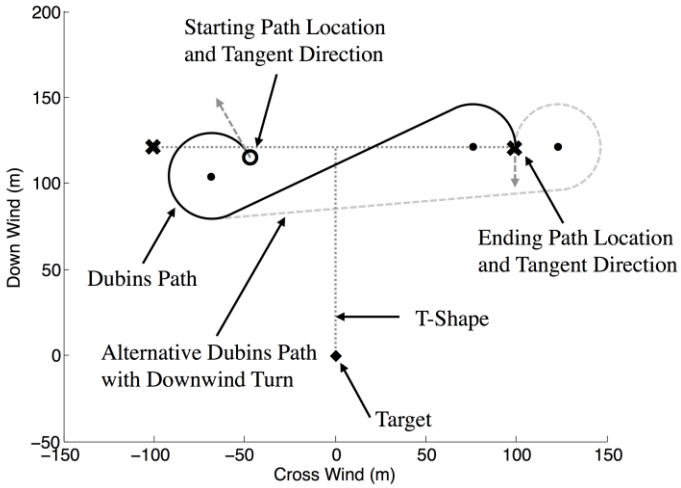

Figure 5: Loiter strategy and T-shaped pattern.

During loiter, the altitude required to reach the target is continually updated each control cycle. This computation is performed based on the current estimate of the system airspeed and descent rate and the calculated instantaneous distance from the target defined as a circular arc of constant radius from the current vehicle heading until the vehicle faces directly toward the target and a straight line segment between the end of this arc and the target. From these two maneuvers, the total distance L to the target and the altitude required to reach the target h_{req} from any point are defined in Equations 4 and 5, respectively.

$$L = |d\psi|R + \sqrt{(x_1 - x_T)^2 + (y_1 - y_T)^2} \tag{4}$$

$$h_{req} = L\frac{\dot{z}}{V_0} \tag{5}$$

Note $d\psi$ is the required change in vehicle heading needed to point at the target, R is the constant turn radius, (x_1, y_1) are the end point coordinates of the circular arc, and (x_T, y_T) are the target coordinates. Once the altitude required drops below the current vehicle altitude, the guidance algorithm transitions from loiter to final approach.

Final Approach

A two-stage final approach technique is employed where the parafoil and payload system initially begins tracking to an offset target following loiter before transitioning to the actual desired impact point. This technique is intended to prioritize landing of the vehicle pointing into the estimated wind vector. The offset target is located directly downwind of the actual target at an altitude intersecting the average glide path of the system. Note the average glide path is defined as the value centered within the longitudinal control range of the vehicle. Accordingly, any perturbation or disturbance from the average glide path ensures that sufficient longitudinal control authority remains to bring the system back to the intended trajectory necessary to intersect the target.

During final approach, the instantaneous distance to the target is continually updated in a manner similar to that employed during loiter. Using this distance estimate combined with altitude feedback, an estimate for the required vehicle glide path necessary to intersect either the offset target or the actual target (depending on which target the system is tracking to at that time) is obtained. If the system is likely to overshoot the intended target, a proportional control strategy is implemented where the upper surface canopy spoilers are subsequently opened thus temporarily increasing the vehicle sink rate and allowing the system to "drop" down onto the correct glide path. All distance calculations are performed within the wind fixed reference frame such that the required glide path is relative to the atmosphere and wind compensation is automatically included.

Terminal Guidance

The guidance logic transitions from final approach to terminal guidance at the instant the altitude of the vehicle drops below the height of the offset target. Recall the offset target is located directly downwind of the desired impact point at an altitude intersecting the average glide of the vehicle. The idea behind this technique is that if the vehicle reaches the offset target at the correct altitude, the remaining portion of the descent will focus primarily on traversing the stem of the T-shaped pattern while maintaining the proper heading and glide path necessary to intersect the target. Vehicle altitude and instantaneous distance from the target are continually updated each control cycle during terminal guidance such that a continuous longitudinal control signal is generated and subsequently mapped to the appropriate level of symmetric spoiler deflection. Figure 6 provides a graphical depiction of the terminal guidance strategy for a simplified trajectory. Note that if terminal guidance is entered either above the minimum glide path or below the maximum glide path, the vehicle will inevitably overshoot or land short of the intended target, respectively. In this case, the guidance logic will simply saturate the symmetric spoiler control while simultaneously keeping the vehicle pointed either at the target or directly upwind of the target in an effort to minimize miss distance.

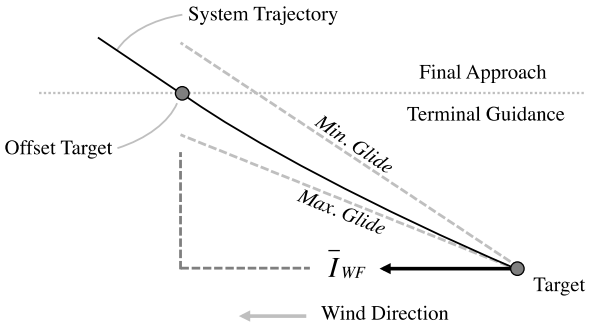

Figure 6: Terminal guidance strategy.

B. Navigation

Following the open-loop initialization maneuver, the navigation algorithm is tasked with continually updating estimates of the atmospheric wind vector and current vehicle heading and heading rate using available sensory information. The estimation process uses a discrete extended Kalman filter (EKF) observer based on the solution of the vector diagram shown in Figure 7. Decomposition of the measured vehicle ground track vector into airspeed (V_0) and wind vector (V_W) components is not unique. Consequently, vehicle airspeed is assumed constant throughout the entire flight. Additionally, solution of the vector diagram in Figure 7 does not yield an estimate of the parafoil heading angle ψ directly, but rather the azimuthal angle χ_0. However, the system sideslip angle β is typically small for parafoil and payload aircraft in which case the azimuthal angle is assumed to be equal to the actual heading angle.

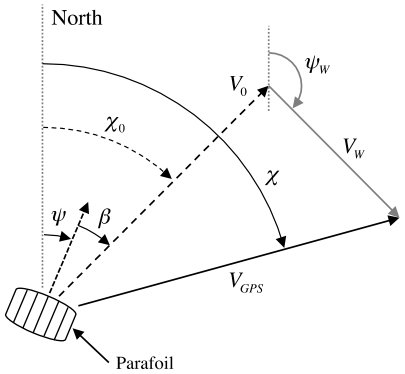

Figure 7: Parafoil ground track velocity decomposition.

C. Control

The parafoil and payload system is controlled via opening and closing the upper surface bleed air spoilers. Based on the current waypoint target supplied by the guidance algorithm and the estimated vehicle location within the wind fixed reference frame, a commanded heading angle ψ_c is computed and subsequently passed to a proportional-integral (PI) controller in order to track the desired heading. Note the proportional component is nonlinear such that control effort resulting from small errors in system heading is reduced. Comparing the commanded heading angle with the filtered estimate of the current vehicle heading ψ_{nav}, a commanded turn rate $\dot{\psi}_c$ is computed according to Equations 6 and 7.

$$\Delta\psi_{ratio} = \frac{\psi_c - \psi_{nav}}{\Delta\psi_{max}} \tag{6}$$

$$\dot{\psi}_c = \begin{cases} \dot{\psi}_{max} & if\ \Delta\psi_{ratio} \geq 1 \\ -\dot{\psi}_{max} & if\ \Delta\psi_{ratio} \leq -1 \\ \dot{\psi}_{max}\Delta\psi_{ratio}\sqrt{|\Delta\psi_{ratio}|} & else \end{cases} \tag{7}$$

Note $\Delta\psi_{max}$ is the maximum difference between the commanded and current vehicle heading after which saturation occurs, and $\dot{\psi}_{max}$ is the maximum allowable vehicle turn rate in either direction. From this commanded turn rate, the required asymmetric spoiler deflection is determined according to Equation 8 were the function *F* is the known vehicle turn rate mapping determined through prior system identification and δa_{bias} is the integral gain component accounting for any unexpected turn bias during flight. Without loss of generality, the resulting asymmetric spoiler input δa is presented as a non-dimensional number within the range $[-1, 1]$ where either extreme represents the maximum asymmetric turning input in either direction for the given vehicle.

$$\delta a = F(\dot{\psi}_c) + \delta a_{bias}, \quad \delta a \in [-1, 1] \tag{8}$$

In addition to lateral turning control, longitudinal control is computed exclusively during the last two phases of flight, namely final approach and terminal guidance. As previously mentioned, a proportional longitudinal control strategy is used during final approach and terminal guidance in which the system attempts to maintain its average glide path necessary to intersect the intended target. Accordingly, Equation 9 is used to compute commanded glide slope (denoted GS_c) where GS_c is confined within the interval $[GS_{min}, GS_{max}]$.

$$GS_c = \begin{cases} GS_{min} & if\ {}^{L}/_{h} \leq GS_{min} \\ GS_{avg} + K_{GS}\left({}^{L}/_{h} - GS_{avg}\right) & if\ GS_{min} < {}^{L}/_{h} < GS_{max} \\ GS_{max} & if\ {}^{L}/_{h} \geq GS_{max} \end{cases} \tag{9}$$

Note that GS_{max}, GS_{min}, and GS_{avg} correspond to the maximum, minimum, and average values of system glide slope, L is the instantaneous distance from the target, h is the current vehicle altitude, and K_{GS} is the glide slope

proportional gain. Using the commanded values of vehicle turn rate and glide slope, the correct combination of asymmetric spoiler input (δa) and symmetric spoiler input (δs) are computed according to the known glide slope and turn rate mapping, denoted as the function H, shown in Equation 10. In practice, this mapping is often implemented as a simple 2D table lookup based on previous flight data and system identification.

$$\delta a, \delta s = H\left(GS_c, \dot{\psi}_c\right), \quad \delta a \in [-1, 1], \quad \delta s \in [0, 1] \tag{10}$$

IV. Test Vehicle Description and System Identification

The small scale test vehicle shown in Figure 8 consists of a rectangular planform canopy attached to a small propeller driven payload. Total canopy surface is 0.98 m^2 (10.5 ft^2) with an aspect ratio of 2.6 and a total system weight of 2.1 kg. Note the system was designed to be hand-launched and features an electric motor and propeller for powered flight, two servo actuators for control line actuation, and an onboard flight computer and sensing suite for executing autonomous flight algorithms. An 18-cell canopy was used where 4 cells on either side of the center section (8 cells total) were configured to include upper surface canopy spoilers as shown in Figure 8b. Each canopy spoiler is actuated by a single control line attached to the leading edge side of the upper surface opening and runs down through the bottom surface of the canopy to the payload where it connects to one of the two servo winch actuators. Note the 4 cells on each side of the center section were connected together for simplicity requiring only two separate servo winch actuators for independent actuation of the left and right bleed air spoiler openings. Once the system reaches the desired altitude under powered flight, the motor and propeller are powered off transitioning the system to gliding descent until landing.

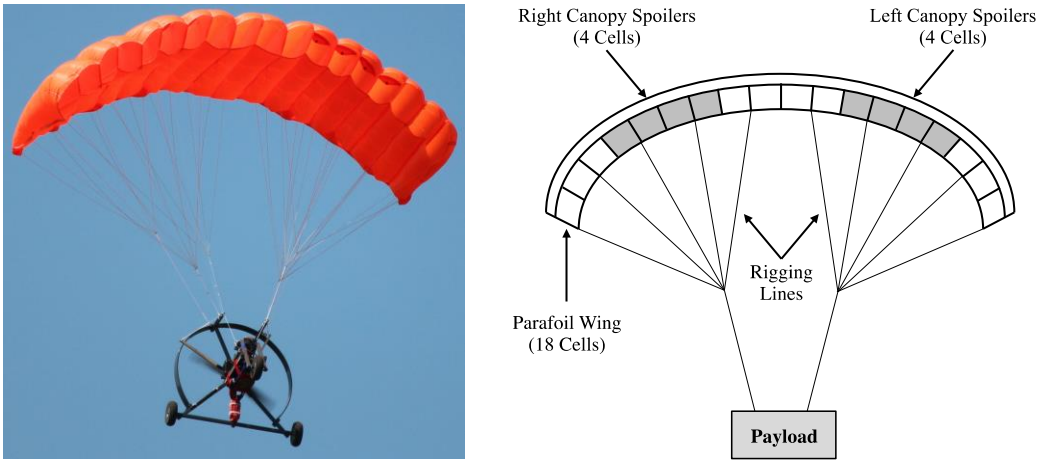

(a) **(b)**

Figure 8: (a) Test vehicle during gliding flight, and (b) upper surface spoiler configuration (front view).

Figure 9 shows the measured steady-state turn rate of the test vehicle as a function of normalized asymmetric spoiler deflection with dashed lines representing typical turn rate limits for autonomous flight (±15 deg/s). Note the asymmetric spoiler deflection was normalized using the actuator maximum deflection as opposed to the maximum turn rate of the vehicle. The measured turn rate is highly nonlinear with a reduced sensitivity to asymmetric input near zero deflection and rapidly increasing turn rate response nearing 40% of the maximum actuator travel in either direction. This significant increase in turn rate sensitivity between 20-40% actuator deflection is likely the result of opening the upper surface bleed air vents beyond their maximum opening and subsequently deforming or "creasing" the upper surface of the canopy.

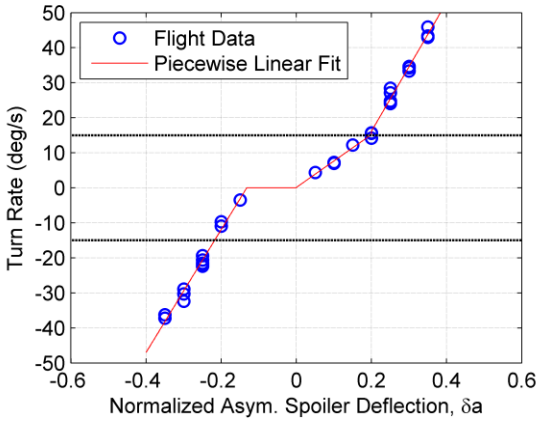

Figure 9: Measured test vehicle turn rate vs. normalized asymmetric spoiler deflection.

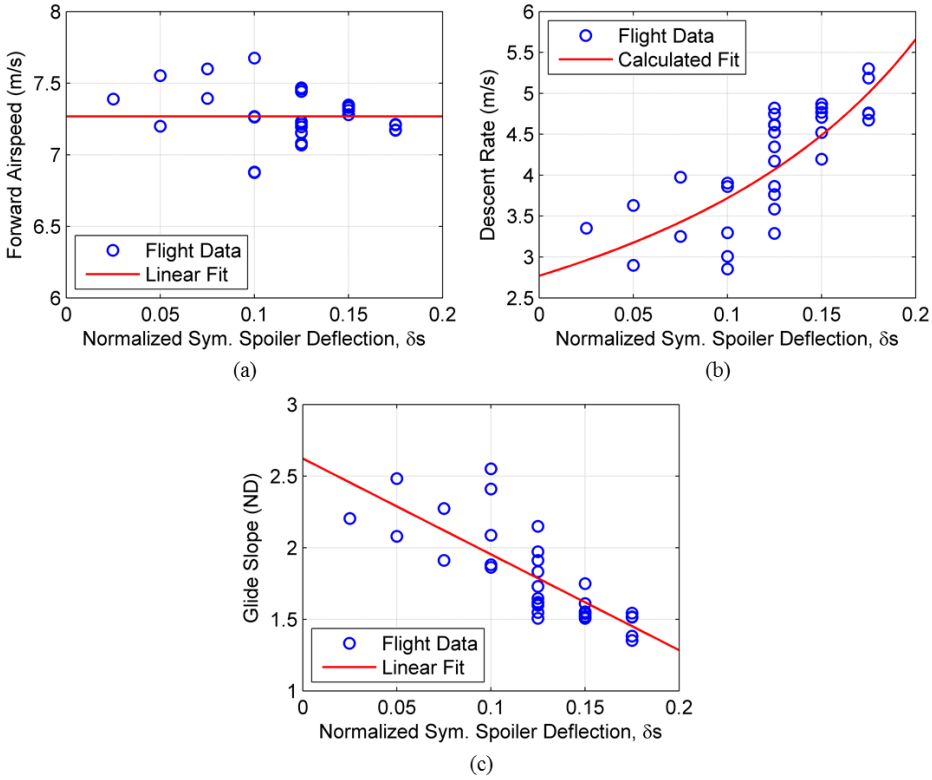

Figure 10: Steady-state flight characteristics vs. normalized symmetric spoiler deflection including (a) airspeed, (b) descent rate, and (c) glide ratio.

In addition to lateral turning performance, several system identification flights were performed specifically focused on measuring the vehicle steady-state longitudinal response (i.e. airspeed, descent rate) as a function of symmetric spoiler input. These results are presented in Figure 10 as a function of normalized symmetric spoiler deflection δs. Estimated airspeed values were largely inconsistent ranging from a minimum of 6.8 m/s to a maximum 7.7 m/s (7.3 m/s average). This inconsistency in airspeed is directly related to the difficulty in obtaining accurate wind estimates. However, significant changes in descent rate with increasing symmetric spoiler deflection were noted resulting in a nominal value of approximately 3.0 m/s with no control input (i.e. spoilers fully closed) to over 5.0 m/s at near maximum usable symmetric deflection. Shown in Figure 10c, the longitudinal control authority of the upper surface bleed air mechanism is capable of reducing the test vehicle glide ratio by over 40% from

approximately 2.6 to less than 1.5. Using this steady-state data, lift and drag coefficients versus angle of attack were estimated for several different levels of normalized symmetric spoiler deflection. These models were primarily used in constructing an accurate representation of the vehicle flight characteristics for purposes of simulation.

V. Autonomous Landing Performance

The following sections investigate the autonomous landing performance of the test vehicle in both simulation and experimental flight tests. Note all simulations and flight tests were perfumed using the upper surface bleed air spoilers exclusively for control. Landing accuracy statistics are presented for both lateral steering only and combined lateral and longitudinal control techniques.

A. Simulation Results

Using the results from the previous system identification process discussed in Section IV, a rigid body, 6 degree-of-freedom (6-DOF) simulation model was developed in which the aerodynamic and control input parameters were tuned to match the steady-state flight characteristics and typical turn rate dynamics of the test vehicle observed in flight. This type of dynamic simulation model is commonly used in modeling aerospace vehicles including parafoil and payload aircraft. Derivation and validation of the 6-DOF simulation model can be found in [19]. Utilizing this computer model, complete autonomous landings were simulated from release altitude to ground impact in a variety of realistic atmospheric conditions allowing for both refinement of the autonomous control logic and evaluation of the expected landing performance.

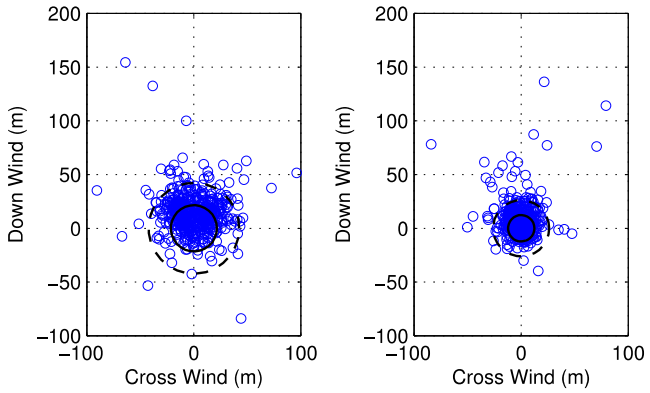

Figure 11: Simulated landing dispersion for lateral only control (left) and combined lateral and longitudinal control (right).

Accordingly, a series of Monte Carlo simulations were performed in which 500 autonomous landings were simulated where the mean wind speed was allowed to vary uniformly from 0-5 m/s (approximately 70% of the vehicle flight speed) and the turbulence level, defined as the standard deviation of the vertical gust component in the Dryen turbulence model [21], was varied uniformly from 0 - 0.75 m/s. Figure 11 presents the simulated landing accuracy dispersion for both lateral steering control only and combined lateral and longitudinal control where impact point errors have been rotated into a down wind / cross wind reference frame. Solid and dashed black lines represent the 50% and 90% circular error probable (CEP) regions, respectively, where the CEP is defined as the minimum radius centered at the target that encompasses 50% or 90% of all recorded landings. Note CEP values are commonly used within the airdrop community for reporting aggregate landing accuracy performance of various systems. Landing accuracy statistics indicate a 43% reduction in 50% CEP when using the combined lateral and longitudinal control (21.5 m lateral only, 12.3 m combined lateral and longitudinal). Similarly, a 38% reduction in 90% CEP was also computed (42.3 m lateral only, 26.2 m combined lateral and longitudinal control). Additionally, Figure 12 illustrates the control input time history for the terminal phase of an example flight. Note the application of symmetric bleed air spoiler actuation allowing the vehicle to systematically “bleed” altitude and maintain the proper glide path necessary to intersect the intended target.

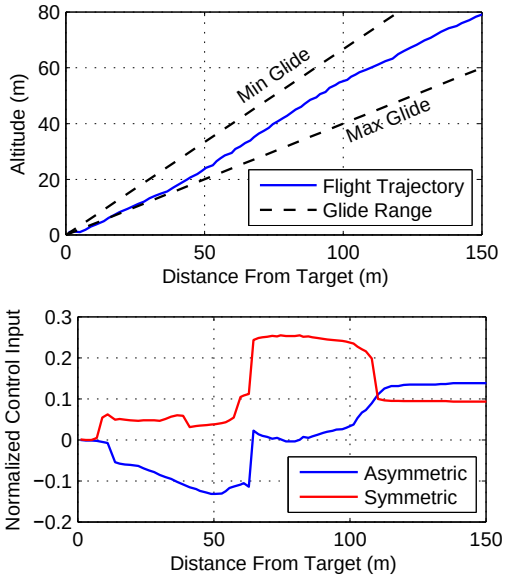

Figure 12: Altitude (top) and normalized control input (bottom) versus instantaneous distance from target for example autonomous flight trajectory.

B. Experimental Flight Test Results

In an effort to validate the simulation model, a total of 70 autonomous landings were recorded over four days of testing in Eloy, Arizona under a variety of wind conditions ranging in average wind speeds of 7 m/s or less with moderate thermal activity and wind shear conditions. For each landing, the test vehicle described in Section IV was hand launched and manually piloted during powered climb to an altitude of approximately 400 m. At this point, the electric motor was stopped and the onboard flight computer was activated for autonomous guided descent and landing. Figure 13 illustrates flight testing operations where two parafoil and payload systems are shown in the foreground next to the target immediately following landing. Note the operator vehicle and ground station location are visible in the background.

Figure 13: Flight operations in Eloy, AZ.

Total miss distance was calculated based on the GPS location of the intended target and the measured position of the parafoil and payload system immediately following impact. Figure 14 presents both the landing dispersion for

all 70 autonomous flights using combined lateral and longitudinal control logic and a comparison of landing error with mean wind speed estimated over the entire flight. Values for the 50% and 90% CEP regions were calculated to be 13.1 m and 28.8 m, respectively. Additionally, Table 1 provides a tabulated summary of both the simulation and experimental flight test performance including comparison with lateral only control and combined lateral and longitudinal control cases.

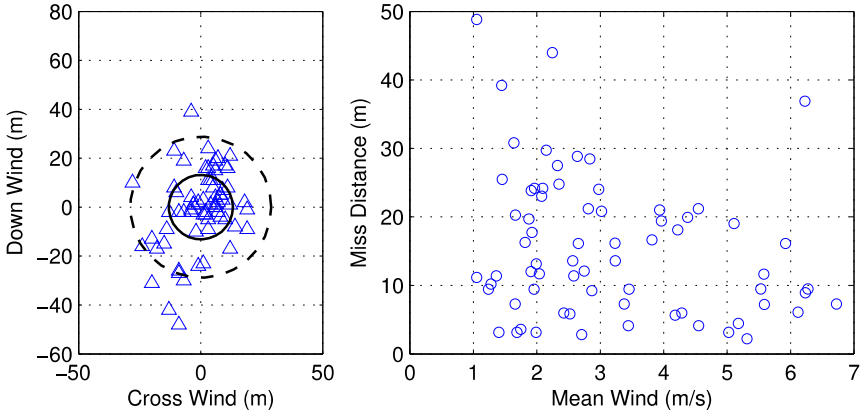

Figure 14: Experimental landing dispersion (left) and calculated miss distance versus mean wind speed (right) for 70 autonomous flight tests using combined lateral and longitudinal control.

As indicated from the simulation and experimental landing accuracy results, it is clear that upper surface canopy spoilers are a viable control mechanism for autonomous parafoil and payload aircraft. Note the simulation and experimental 50% CEP values are very consistent at 12.3 m and 13.1 m, respectively, indicating excellent model agreement with the test vehicle as well as realistic atmospheric conditions. In short, the autonomous system clearly demonstrates the capability to leverage the added control authority of the combined lateral and longitudinal control logic using upper surface bleed air spoilers to compensate for imperfect approach trajectories and other outside disturbances in order to land accurately.

Table 1: Simulated and experimental landing accuracy statistics.

Metric Description	50% CEP (m)	90% CEP (m)	Reduction in 50% CEP
Simulation – Lateral Only (500 Landings)	21.5	42.3	--
Simulation – Combined Lat/Lon (500 Landings)	12.3	26.2	43%
Flight Tests – Lateral Only (31 Landings)	25.6	51.0	--
Flight Tests – Combined Lat/Lon (70 Landings)	13.1	28.8	49%

VI. In-Canopy Bleed Air Actuation System

A large portion of size, weight, and cost of the AGU used for autonomous flight in currently fielded systems is dedicated to electric winch actuators and batteries in order to satisfy the significant torque and power requirements needed to deform large portions of the canopy trailing edge for control. However, bleed air spoilers require considerably less actuation force to deform the upper canopy surface and subsequently open the bleed air vents. As a result, a significant research effort has recently begun focusing on the design and development of a complete in-canopy (wireless) bleed air actuation system for large parafoil aircraft in order to not only reduce the cost, size, and rigging complexity of conventional systems, but also increase the control effectiveness, performance, and landing accuracy of autonomous systems through bleed air control. The in-canopy actuation system consists of several small, specifically designed winch actuators mounted entirely within the parafoil canopy capable of opening one or more bleed air vents completely independent of the system AGU. A total of 28 test flights have been conducted

using the in-canopy actuation hardware in conjunction with the Natick Soldier Research Development and Engineering Center (NSRDEC) Airdrop Technology team from June 2014 through January 2015 in Eloy, Arizona.

A. In-Canopy Actuator Design

The key component of the in-canopy actuation system is the servo winch actuator itself. Designed for robust operation with minimal size and weight, the in-canopy actuator is comprised of a single cylindrical tube housing all internal components including a brushed DC gear motor, control line spool and bearing, battery pack, wireless transceiver, and motor driver electronics. An exploded view of the in-canopy actuator and associated parts is shown in Figure 15. Overall length of the in-canopy actuator is 7.25 inches with an outside diameter of 1.25 inches. Total weight for one actuator including battery is 8.0 ounces. Rounded end caps were also added to minimize the possibility of any sharp edges tearing through the canopy fabric during packing or opening of the parachute.

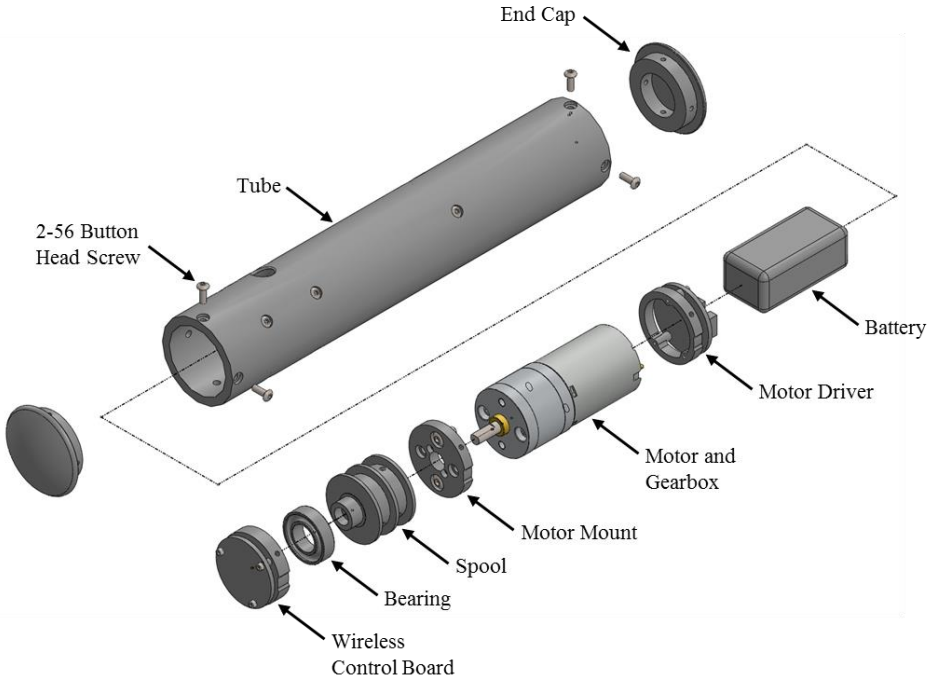

Figure 15: In-canopy actuator exploded component view.

The mounting strategy of the actuator within the canopy itself is shown in Figure 16 where the actuator is secured at the intersection of the structural rib and lower canopy surface at the point where the rigging line attachment point is located. Those areas on the lower surface nearest rigging line attachment points are considered "hard points" within the canopy and provide the most rigid foundation for securing hardware. In practice, six button-head type fasteners and grommets were used to secure each actuator in place. The internal control line rigging configuration is also shown in Figure 16 where the control line first exits the actuator and goes directly up to the bleed air vent where it passes through a small ring attached to the leading edge side of the opening before running back down and securing at the intersection between the adjacent structural rib and lower surface. As the in-canopy actuator reels in line, the ring attached to the bleed air opening is subsequently "pulled" downward as the tension in the control line increases. Similarly, as the actuator releases or reels out control line, the internal pressure within the cell and spanwise tension in the canopy forces the bleed air opening closed preventing any further airflow to the outside of the cell. One advantage to rigging the control lines in this configuration is that line tension is distributed equally between adjacent structural ribs minimizing any deformation of the lower canopy surface. Adjacent half-cells can also be actuated using only one in-canopy actuator fitted with two control lines. In this case, a single hole in the structural rib nearest the in-canopy actuator is added allowing the second control line to pass through to the adjacent half-cell.

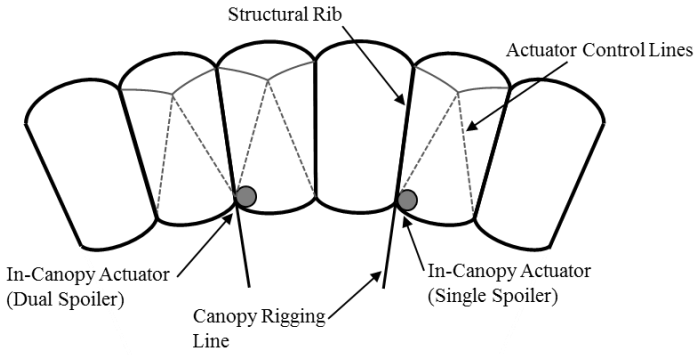

Figure 16: In-canopy actuator mounting and control line rigging configuration.

Each in-canopy is equipped with a low-power, 2.4 GHz wireless communication interface allowing transmission of individual deflection commands to each actuator from a central transmitter attached to the system AGU. This central transmitter, termed the payload relay box, serves to "relay" individual spoiler deflection commands either computed locally or received from the ground station graphical user interface (GUI) via a 900 MHz long range wireless transceiver to each individual actuator installed within the parafoil canopy. During flight, the 2.4 GHz wireless link between the payload relay box and each individual actuator serves to create a simple point-to-point communication network in which each in-canopy actuator is a unique network address and individually addressable by the central transmitter. Figure 17 illustrates this simple wireless network topology of the in-canopy actuation system.

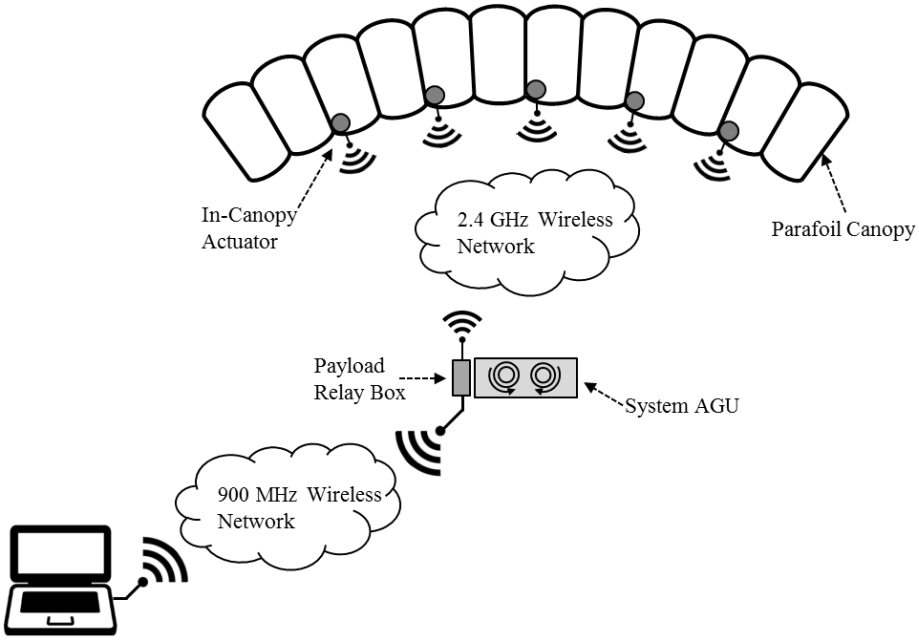

Figure 17: In-canopy actuation system wireless network topology.

Also housed inside the payload relay box is a microprocessor, GPS receiver and antenna, barometric pressure sensor, and adequate non-volatile storage capacity for in-flight data logging and program storage. Under manual (i.e. R/C) control, individual spoiler deflection commands specified by the user are sent up to the payload relay box and subsequently retransmitted to each in-canopy actuator. However, the payload relay box can also be configured for fully autonomous operation in which all spoiler deflection commands are computed locally by the internal microprocessor and sensing suite. Transitioning between manual and autonomous flight is controlled from the

ground station GUI and can be changed at any point during flight. Figure 18 shows both the payload relay box mounted to an AGU and one of the in-canopy actuators installed within an MC-4/5 canopy prior to test flight.

(a) (b)

Figure 18: (a) Payload relay box mounted on MC-4/5 AGU, and (b) in-canopy actuator mounted within MC-4/5 canopy prior to test flight.

B. Flight Testing

Initial flight testing of the in-canopy bleed air spoiler actuation system began in June 2014 in Eloy, Arizona, with the goal of verifying not only the actuator mounting design and survivability of all associated hardware, but also the ad-hoc wireless communication scheme between the ground station GUI, payload relay box, and each individual in-canopy actuator. As of January 2015, a total of 28 flight tests have been conducted using the in-canopy bleed air actuation system. Each subsequent test has continued to advance the performance and robustness of the in-canopy hardware with the ultimate goal of developing a reliable and effective alternative to bleed air control using payload centric actuators.

Of the 28 total test flights, 20 flights were performed with the MC-4/5 system including two fully autonomous flights from canopy opening to ground impact. The MC-4/5 parachute, shown in Figure 19 is a personnel parachute with a total surface area of 370 ft^2. Total weight of the autonomous system including parachute and all in-canopy hardware is 376 lb. Also shown in Figure 19 is a view from inside one of the canopy cells of the MC-4/5 during flight further depicting the in-canopy actuator mounting and control line rigging configuration.

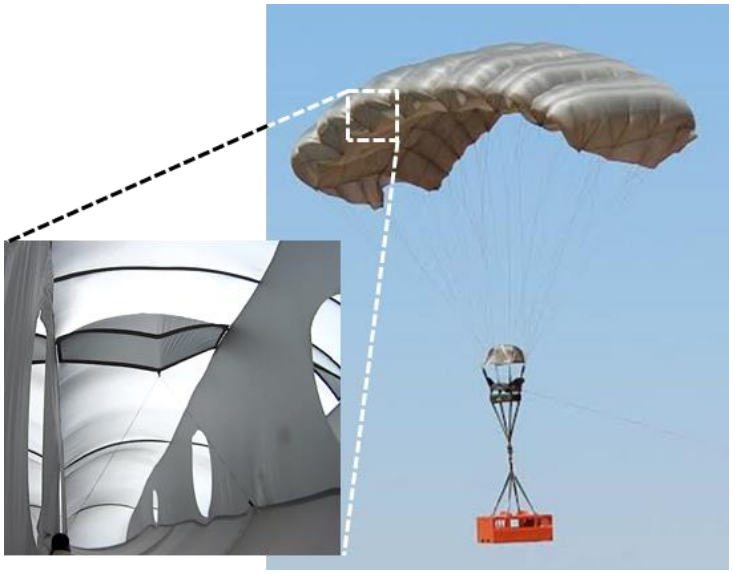

Figure 19: MC-4/5 parafoil canopy and internal view of in-canopy actuator.

For all test flights using in-canopy hardware, the system AGU and trailing edge brake control lines were left in place for safety thus maintaining the ability to fly autonomously or from manual control using the AGU flight software if needed. Testing protocol for the MC-4/5 and all other systems using in-canopy actuators consisted of first allowing the parachute to fully open upon exiting the aircraft and the AGU to complete its initialization procedure before transitioning the AGU flight software to manual control with zero deflection of the trailing edge. At that point, the system is under complete control from the in-canopy actuators and capable of executing manual scripts or autonomous flight.

A series of system identification flights were performed with the MC-4/5 canopy to quantify the steady-state flight characteristics using the in-canopy bleed air actuation system. Note a total of 6 in-canopy actuators were installed within the canopy (3 on either side of the canopy centerline) resulting in a total of 10 actuated upper surface bleed air vents. Figure 20 shows the estimated vehicle turn rate magnitude versus vertical deflection of the upper surface opening for three different asymmetric spoiler configurations. The shaded cells shown in Figure 20 correspond to those in which the upper surface bleed air vents were used for control. In the case of only one actuator, only the furthest outboard spoiler was actuated. When using both two and three actuators, three and five outboard spoilers were actuated, respectively. Maximum turn rate achieved using three in-canopy actuators (5 bleed air spoilers) was approximately 18 deg/s providing more than sufficient lateral control authority for autonomous flight. Also, a significant deadband exists where approximately 2 inches of vertical displacement of the bleed air opening is needed before any measureable turn rate is detected. This existence of turn rate deadband is likely the result of small displacements of the bleed air opening separating only the sealing flap from the canopy upper surface without actually opening the bleed air vent.

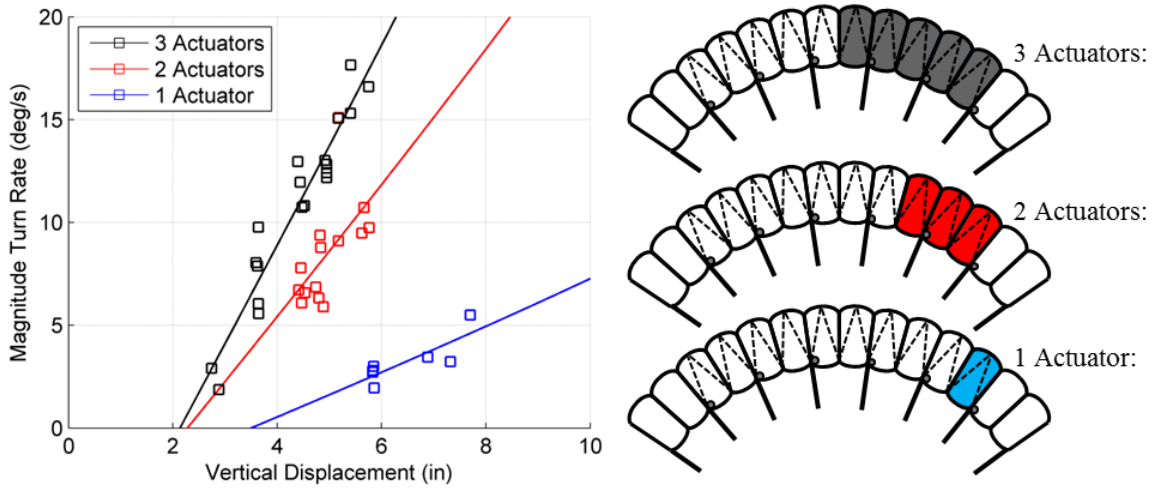

Figure 20: MC-4/5 measured turn rate versus vertical displacement of the upper surface bleed air opening.

Figure 21 shows estimated horizontal airspeed and descent rate as a function of vehicle turn rate. All velocity values have been scaled to their indicated (i.e. sea-level) equivalent. Although minimal change in horizontal airspeed of the vehicle was evident from flight data, the estimated change in glide slope of the MC-4/5 during turning flight was over 30% ranging from a maximum value of approximately 2.3 to a minimum of 1.6. Additional testing is needed to confirm the maximum achievable change in glide slope during straight flight where all upper surface bleed air spoilers are fully opened (i.e. maximum symmetric control input). In this configuration, a reduction in glide slope by 50% or more is expected.

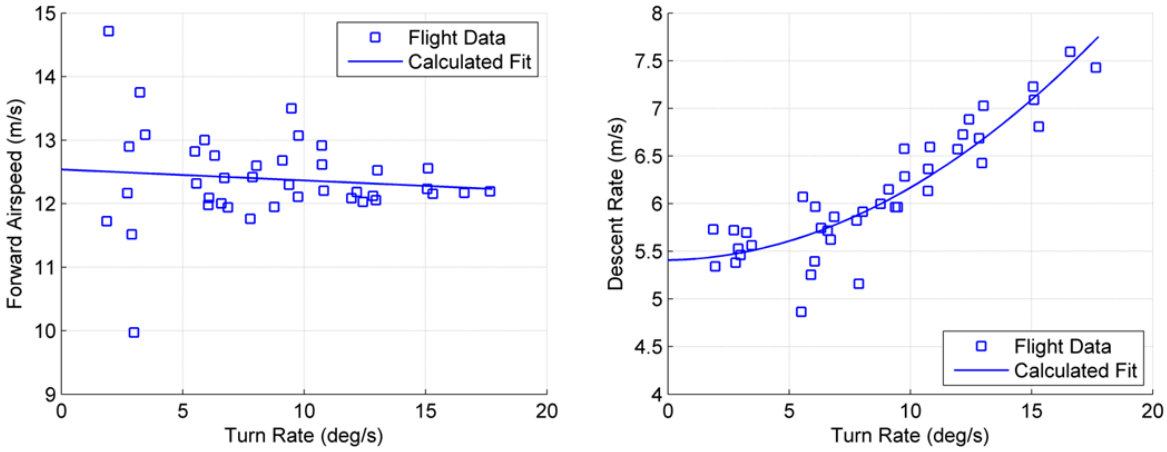

(a) (b)

Figure 21: MC-4/5 (a) airspeed and (b) descent rate versus turn rate.

VII. Conclusions

It has been shown that upper surface bleed air spoilers are a viable mechanism for lateral and longitudinal control of parafoil and payload aircraft during autonomous flight. Using a specialized GN&C algorithm designed to leverage the added control authority of upper surface bleed air spoilers, a substantial reduction in median miss distance of nearly 50% was noted in both high-fidelity computer simulation and experimental flight tests using a small scale parafoil and payload test vehicle. Median miss distance for all 70 autonomous flights using the small scale test vehicle equipped with upper surface bleed air spoilers and combined lateral and longitudinal control logic was 13.1 m. Additionally, a novel in-canopy bleed air actuation has been developed and successfully flight tested on a variety of large parafoil systems including the MC-4/5 with excellent results. The in-canopy actuation system consists of several small, specifically designed winch actuators mounted entirely inside the parafoil canopy capable of opening one or more bleed air vents independent of the system AGU via a unique internal rigging structure. Individual deflection commands for each in-canopy actuator are transmitted wirelessly from the payload completely eliminating the need for any control lines or motors within the AGU. To date, two successful autonomous flights with the MC-4/5 from canopy opening to ground impact have been completed demonstrating the capability of the in-canopy actuation system. Future work includes optimization of the upper surface bleed air vent design in order to increase control authority and therefore reduce the number of required in-canopy actuators further minimizing the overall footprint of the in-canopy actuation hardware.

VIII. Acknowledgements

The authors would like to acknowledge the support of the Natick Soldier Research Development and Engineering Center (NSRDEC) Airdrop Technology Team and also Frank Deazley of Aerial Delivery Solutions LLC.

IX. References

[1] Calise, A. J. and Preston, D., "Swarming/Flocking and Collision Avoidance for Mass Airdrop of Autonomous Guided Parafoils," Journal of Guidance, Control, and Dynamics, Vol. 31, No. 4, 2008, pp. 1123-1132. doi: 10.2514/1.28586

[2] Carter, D., George, S., Hattis, P., Singh, L., and Tavan S., "Autonomous Guidance, Navigation, and Control of Large Parafoils," AIAA Paper 2005-1643, May 2005. doi:10.2514/6.2005-1643

[3] Carter, D., George, S., Hattis, P., McConley, M., Rasmussen, S., Singh, L., and Tavan S., "Autonomous Large Parafoil Guidance, Navigation, and Control System Design Status," AIAA Paper 2007-2514, May 2007. doi:10.2514/6.2007-2514

[4] Carter, D., Singh, L., Wholey, L., Rasmussen, S., Barrows, T., George, S., McConley, M., Gibson, C., Tavan S., and Bagdonovich, B. "Band-Limited Guidance and Control of Large Parafoils," AIAA Paper 2009-2981, May 2009. doi:10.2514/6.2009-2981

[5] Jann, T., "Advanced Featured for Autonomous Parafoil Guidance, Navigation, and Control," AIAA Paper 2005-1642, May 2005. doi:10.2514/6.2005-1642
[6] Kaminer, I. I. and Yakimenko, O. A., "Development of Control Algorithm for the Autonomous Gliding Delivery System," AIAA Paper 2003-2116, May 2003. doi:10.2514/6.2003-2116
[7] Murray, J. E., Sim, A. G., Neufeld, D. C., Rennich, P., Norris, S., and Hughes, W., "Further Development and Flight Test of an Autonomous Precision Landing System Using a Parafoil," NASA TM-4599, July 1994; also AIAA Paper 1994-2141, July 1994. doi:10.2514/6.1994-2141
[8] Slegers, N. J. and Yakimenko, O. A., "Optimal Control for Terminal Guidance of Autonomous Parafoils," AIAA Paper 2009-2958, May 2009. doi:10.2514/6.2009-2958
[9] Calise, A. and Preston, D., "Design of a Stability Augmentation System for Airdrop of Autonomous Guided Parafoils," AIAA Paper 2006-6776, Aug. 2006. doi:10.2514/6.2006-6776
[10] Yakimenko, O. A., Slegers, N. J., and Tiaden, R. A., "Development and Testing of the Miniature Aerial Delivery System Snowflake," AIAA Paper 2009-2980, May 2009. doi:10.2514/6.2009-2980
[11] Slegers, N. and Costello, M., "On the Use of Rigging Angle and Canopy Tilt for Control of a Parafoil and Payload System," AIAA Paper 2003-5609, Aug. 2003. doi:10.2514/6.2003-5609
[12] Ward, M., Culpepper, S., and Costello, M., "Parafoil Control Using Payload Weight Shift," Journal of Aircraft, Vol. 51, No. 1, 2014, pp. 204-215. doi:10.2514/1.C032251
[13] Bergeron, K., Fejzic, A., and Tavan, S., "AccuGlide 100: Precision Airdrop Guidance and Control via Glide Slope Control," AIAA Paper 2011-2530, May 2011. doi:10.2514/6.2011-2530
[14] Slegers, N., Beyer, E., and Costello, M., "Use of Variable Incidence Angle for Glide Slope Control of Autonomous Parafoils," Journal of Guidance, Control, and Dynamics, Vol. 31, No. 3, 2008, pp. 585-596. doi:10.2514/1.32099
[15] Ward, M. and Costello, M., "Adaptive Glide Slope Control for Parafoil and Payload Aircraft," Journal of Guidance, Control, and Dynamics, Vol. 36, No. 4, 2013, pp. 1019-1034. doi:10.2514/1.59260
[16] Bergeron, K., Ward, M., and Costello, M., "Aerodynamic Effects of Parafoil Upper Surface Bleed Air Actuation," AIAA Paper 2012-4737, Aug. 2012. doi:10.2514/6.2012-4737
[17] Gavrilovski, A., Ward, M., and Costello, M., "Parafoil Control Authority with Upper-Surface Spoilers," Journal of Aircraft, Vol. 49, No. 5, 2012, pp. 1391-1397. doi:10.2514/6.2011-2517
[18] Goodrick, T. F., Pearson, A., Murphy, A. L., Jr., "Analysis of Various Automatic Homing Techniques for Gliding Airdop Systems with Comparative Performance in Adverse Winds," AIAA Paper 73-462, May 1973.
[19] Ward, M., Costello, M., and Slegers, N., "Specialized System Identification for Parafoil and Payload Systems," Journal of Guidance, Control, and Dynamics, Vol. 35, No. 2, 2012, pp. 588-597. doi:10.2514/1.53364
[20] Dubins, L. E., "On Curves of Minimal Length with a Constraint on Average Curvature, and with Prescribed Initial and Terminal Positions and Tangents," American Journal of Mathematics, Vol. 79, No. 3, 1979, pp. 497-516.
[21] Military Standard, *Flying Qualities of Piloted Aircraft*, 1990, MIL-STD-1797A.